Experimental constraints on miscibility gap between apatite and britholite and REE partitioning in an alkaline melt

Revision 2

Aleksandr S. Stepanov[1*], Irina A. Zhukova[1], Shao-Yong Jiang[1]

[1]*State Key Laboratory of Geological Processes and Mineral Resources, Collaborative Innovation Center for Exploration of Strategic Mineral Resources, Faculty of Earth Resources, China University of Geosciences, Wuhan 430074, China,*

Abstract

Apatite containing 14 wt.% TREO (total rare earth oxide) and coexisting with calciobritholite with 37.2 wt.% TREO have been synthesized at 800 °C and 10 kbar from a felsic melt with the addition of NaCl. The analysis of the experimental products with regression analysis of time resolved (RATR) Laser ablation inductively coupled plasma mass spectrometry (LA-ICP-MS) data allowed to estimate the composition of the coexisting phases. The results suggest that equilibrium has been established during the run and both apatite and calciobritholite contained REE in $[Si^{4+}REE^{3+}]$ to $[Ca^{2+}P^{5+}]$ solid solution, whereas the coupled substitution $[Na^{1+}REE^{3+}]$ to $[2Ca^{2+}]$ was insignificant despite crystallization from an alkaline, Na-rich melt. The coexistence of the apatite and calciobritholite and available experimental data allowed the miscibility gap to be constrained between apatite and calciobritholite, and suggest complete miscibility between apatite and britholite above 950 °C. The melt that produced coexisting apatite and calciobritholite was characterized by a significant Cl

content of (0.51 wt.%) and elevated REE (526 ± 19 ppm Ce) and low P content (112 ± 49 ppm). The change of the accessory mineral association from monazite to apatite and calciobritholite with the addition of NaCl illustrates the importance of halogens for mineral associations. The partition coefficients of britholite are similar to apatite and distinguished mainly by a higher preference for REE and Th. Henry's law was not acting for the total REE content in the melt because of the buffered system, however the partition coefficients could still be used for the prediction of the relative REE patterns for melts that generated high-REE apatite and/or calciobritholite. These results have implications for the interpretation of the phosphate associations in alkaline volcanic and plutonic rocks.

Keywords: apatite, britholite, calciobritholite, REE, alkaline magma, experimental petrology, LA-ICP-MS

Introduction

Britholite is a mineral with an apatite structure and a general formula (Na, Ca, REE)$_{10}$(Si, P)$_6$O$_{24}$(OH, F, Cl)$_2$ defined by the prevalence of REE over Ca. An intermediate species, calciobritholite, distinguished from apatite by Si>P also has been proposed (Pekov et al. 2007). Britholite and calciobritholite are quite common minerals in alkaline rocks and some REE deposits (Pekov et al. 2007; Lorenz et al. 2019). Symplectites composed of apatite matrix and inclusions of REE-rich minerals including britholite, monazite, and other REE minerals have been observed in a series of localities such as the Misery syenitic intrusion, Canada (Petrella et al. 2014), Rodeo de los Molles deposit, Argentina (Lorenz et al. 2019), Nolans Bore, Australia (Anenburg et al. 2018), and the Mushgai-Khudag Complex, Mongolia (Nikolenko et

al. 2018). These symplectites have been interpreted as products of the decomposition of a high-temperature solid solution between apatite and britholite (Anenburg et al. 2018; Lorenz et al. 2019). Synthetic britholite is important for material science as it has been proposed as an actinide host for nuclear waste disposal and is a typical phase in slags after industrial REE extraction (Lan et al. 2021).

Apatite is one of the most common accessory minerals and the REE patterns of apatite is an essential petrologic indicator (Belousova et al. 2002; Zirner et al. 2015; Chakhmouradian et al. 2017; O'Sullivan et al. 2020; Yudovich et al. 2022). Substitution mechanisms involving Na and Si have been identified for REE in apatite (Pan and Fleet 2002). The substitution mechanism for REE likely has a significant effect on the REE thermodynamic properties in apatite, which are critical for the modelling of the behavior of REE during magma evolution, metamorphism, subduction zone devolatilization (Li and Hermann 2017), and nuclear waste disposal (Janots 2008).

Analysis of the products of experiments with accessory minerals could be a challenging endeavor because of the small grain size and complex composition of the phases (Bussweiler et al. 2020; Stepanov et al. 2020). Laser ablation inductively coupled plasma mass spectrometry (LA-ICP-MS) is the method of choice for the analysis of REE in geological samples; however, the fine-grained experimental products are often beyond the technique's spatial resolution. Therefore, a method of regression analysis of time resolved (RATR) LA-ICP-MS data has been developed (Rubatto and Hermann 2007; Stepanov et al. 2012, 2020). Here, we report the results of an experiment conducted with the aim to investigate the effect of NaCl on mineralogy of REE-bearing felsic melt. The RATR of LA-ICP-MS data allowed determining the composition of calciobritholite and apatite. The evaluation of the

74 results from past experimental studies on high-REE apatite and britholite allowed for
75 the inference of implications for the interpretation of similar associations in natural
76 rocks.
77

78 **Methods**

79 **Starting composition and run conditions**

80 The starting material was the same mixture synthesized by a 'sol–gel' method
81 by Stepanov et al. (2012) . The nitrate solutions of major and trace elements (Li, Be,
82 Na, K, Ca, Sc, Ti, Mn, Sr, REE, Zr, Nb, Ba, Hf, Ta and Pb) were mixed with
83 tetraethyl orthosilicate [$Si(C_2H_5O)_4$] and slowly dried to a gel. The starting material
84 was prepared as a mixture of two components (B and Din Table 1 in Stepanov et al.
85 2012) in a proportion that ensured crystallization of a reasonable fraction of accessory
86 minerals. It had the composition of a peraluminous leucogranite with the addition of
87 P, LREE, Th, and U in proportions similar to natural monazite. The HREE were
88 added in greater amounts relative to natural abundances to make concentrations in
89 both the melt and minerals more suitable for analysis. After grinding in an agate
90 mortar, the mix was melted to glass in a platinum crucible at 1400 °C. Aluminium
91 oxide was added to the ground glass afterwards. Approximately 20 mg of powdered
92 starting composition plus 2 mg sodium chloride were placed in a 2.3 mm diameter Pt
93 capsule. Distilled water was added to the capsule by a micro-syringe in an amount
94 equivalent to 16 wt.% H_2O in the melt. The capsule was wrapped in the water-soaked
95 paper tissue, to prevent overheating, and then sealed using an argon torch arc welder.
96 The experiment was performed in an end-loaded 200-ton hydraulic piston-
97 cylinder apparatus at the Research School of Earth Sciences, Australian National

University (RSES, ANU). The heating and pressurization sequence was the same as described in Stepanov et al. (2012). The experimental charge was held at 10 kbar and 800 °C and for seven days. The experiment was quenched by switching the power off.

Electron microscopy and Raman spectroscopy

The experimental capsule was set in epoxy, sectioned, and polished before analyses. Backscattered electron (BSE) images of the sample were collected using a JEOL 6400 scanning electron microscope (SEM) at the ANU Centre for Advanced Microscopy. The content of Ce, La, Nd, and Th in the minerals was estimated by EDS operating at 15 kV and a beam current of 1 nA using a 2 to 3 μm beam spot. The concentrations have been estimated using pure REE phosphates as standards. The composition of the glass was analyzed via EDS by using beam with same parameters as for analysis of minerals for rectangular scans of grain-free areas larger than 5×5 μm, which limited the loss of Na and K during signal acquisition. The acicular shape of the apatite and the calciobritholite crystals (Fig. 1) resulted in some contribution from the glass to the analyses. This issue was alleviated by the subtraction of the glass component (always < 20%) as estimated from the Al content (Watson and Green 1981). After the subtraction of the glass component, the Na_2O content in the apatite and calciobritholite was under 0.1 wt.% (Table 1).

Raman spectra were obtained at the Geoscience Australia using a Raman spectrometer Dilor SuperLabram, with a holographic notch filter (600 and 1800 g/mm gratings), liquid nitrogen-cooled 2000 pixel CCD detector, and a 514.5 nm Melles Griot 543 argon ion laser generating 5 mW on the surface of the sample. The slit width of 100 μm resulted in spectral resolution of 2 cm^{-1}. The microscope was equipped with a 50X ULWD Olympus microscope objective, focusing the laser to a spot 2 μm in diameter.

123

124 **RATR of LA-ICP-MS data**

125 Because of small size of mineral grains (Fig. 1) the direct measurement of
126 composition by LA-ICP-MS was not possible. Therefore, we collected mixed LA-
127 ICP-MS analyses of the melt and the crystals and applied RATR of LA-ICP-MS data
128 for deconvolution of mixed analyses as described by Stepanov et al. (2012, 2020).
129 The difference in this study was that the mixtures of the three components (melt,
130 apatite, and calciobritholite) have been analyzed by RATR of LA-ICP-MS.

131 The LA-ICP-MS analyses were conducted at the Research School of Earth
132 Sciences (ANU) using a pulsed 193 nm ArF Excimer laser coupled to an Agilent 7500
133 quadrupole ICP-MS. Laser sampling was performed in an He–Ar atmosphere at a
134 repetition rate of 5 Hz. Overall, 23 individual spot analyses were collected, including
135 11 spots with a 16 μm diameter and 12 spots with a 25 μm diameter. Data acquisition
136 was performed by peak hopping in pulse counting mode, where individual intensity
137 data for each element was acquired during each mass spectrometer sweep. The list of
138 measured elements included Si, Ca, Al, P, Ti, Mn, Zr, Hf, Nb, Ta, Sr, Ba, Pb, REE,
139 Th, and U. For each analysis, data were collected for 60 s, including the gas
140 background of 25 s. The synthetic NIST610 glass standard, was analyzed before and
141 after each batch of analyses with the corresponding spot size, and used as an external
142 standard with values from Jochum et al. (2011). Element concentrations were
143 calculated by an in-house Excel spreadsheet using the SiO_2 content in the glass, as
144 measured by EDS, as the internal standard.

145 Time-resolved ablation patterns were visually inspected, and segments with
146 variable REE counts used for integration. Data collected with the two different spot
147 sizes gave consistent results and were combined into a dataset of 75 sub-analyses,

148 which were treated as individual measurements in subsequent calculations. The data
149 set was investigated for relations between elements and revealed two trends
150 converging to a cluster of analyses with a low trace element content, corresponding to
151 the melt composition (Fig. 2). The trends have been interpreted as melt-
152 calciobritholite and melt-apatite mixtures. The space between the trends indicated an
153 absence of a mixture of both apatite and calciobritholite in the analyzed spots. The
154 data was divided into two sub-datasets, one composed of melt-apatite mixtures
155 comprising 44 analyses and another containing melt-calciobritholite mixtures with 49
156 analyses. Each population then was treated by the regression analysis with Ce as an
157 independent variable (Stepanov et al. 2012, 2020). The composition of the minerals
158 was estimated from the extrapolation of the regressions to Ce content measured by
159 EDS. The calculations by this RATR algorithm allowed the estimation of all REE, Sr,
160 Pb, Ba, Th, and U in the apatite and calciobritholite (Table 1). Other trace elements
161 present in the starting composition, such as Zr, Hf, Nb, and Ta showed poor
162 correlations with Ce because of their low content in the apatite and calciobritholite.
163 Uncertainties have been calculated at the 90% confidence level as described in
164 Stepanov et al. (2012, 2020). The melt composition (Fig. 3) was calculated by
165 averaging 15 analyses with the lowest REE concentrations. For La, Ce, Nd, and Th
166 the results from RATR LA-ICP-MS analysis showed good agreement with the EDS
167 results.
168

Results

Phase relationships and compositions

The experimental charge was composed of glass, apatite, REE silico-phosphate and salt crystals in cracks (Fig. 1a). Clots of acicular mineral grains were dispersed throughout the glass. The glass was homogeneous and contained small fluid exsolution bubbles. The melt was significantly more alkaline (Alumina Saturation Index ASI=0.84 ± 0.02) than the starting composition (ASI=1.15; Stepanov et al. 2012) and corresponded to trachyte according to the TAS classification (Le Maitre et al. 2002). The melt contained 0.51 ± 0.02 wt.% Cl and the total deficit suggest about 11.6 wt.% of H_2O in the melt (Table 1).

The minerals were identified from major element compositions by EDS and by Raman spectroscopy (Fig. 4). The total REE content was roughly 14 wt.% in the apatite corresponding to about 9% molar Si/(Si + P) and REE/(REE + Ca). For the silico-phosphate, 37.2 wt.% TREO (total rare earth oxide) corresponds to 38% Si/(Si + P) and 28% REE/(REE + Ca). Considering high content of Th, which should be considered "britholite" rather than "apatite" component, these ratios are within the uncertainty of the classification criteria for the silico-phosphates by Pekov et al. (2007) indicating the mineral to be calciobritholite.

The Cl content in the apatite could have been overestimated by EDS analysis because of the diffusion of the halogens under the electron beam (Stormer et al. 1993; Goldoff et al. 2012; Stock et al. 2015). Irrespective of this effect, the measured Cl concentrations of 1.1 wt.% are lower than the theoretical limit of 6.8 wt.% suggesting that OH is present in apatite. Calciobritholite content of 1.1 wt.% Cl is lower than 4.4 wt.% possible in the $Ce_3Ca_2Si_3Cl$ endmember, again suggesting the presence OH. Fluorine was not added to the system and its content in minerals was insignificant.

Low F content distinguished the experimental calciobritholite from natural compositions, which are often characterized by high F (Pekov et al. 2007).

The compositions of minerals and melt were used for the calculation of the partition coefficients as ratios of the element content in mineral divided by the element content in melt (Table 1). The apatite partition coefficient for Th, D_{Th}, is lower than that for U, D_U, and reverse is true for calciobritholite. Both apatite and calciobritholite showed that D_{Th} and D_U are lower than that for Sm, D_{Sm}, and for Gd, D_{Gd}. Apatite and calciobritholite have similar REE patterns, which differ only by a higher REE content in the calciobritholite. The partition coefficient $D_{Sr} = 3$ is close to the range of 4 to 12 obtained by Li and Hermann, (2017), which is also in relative agreement with values of 1.1 to 2.4 obtained by Watson and Green (1981). Barium shows a mild incompatibility in apatite with $D_{Ba} = 0.8$, which is consistent with other data on apatite partitioning (Pan and Fleet 2002).

Raman spectroscopy

The Raman spectra of apatite and calciobritholite are distinctively different. The calciobritholite spectra is characterized by two major bands at 860 cm^{-1} assigned to the ν_1 SiO_4^{2-} vibrations and 956 cm^{-1} that assigned to ν_1 PO_4^{3-} symmetric stretching vibrations (Fig. 3). The ν_4 PO_4^{3-} vibrational bands are present at 580 (with a shoulder appearing at ~ 574 cm^{-1}) and 612 cm^{-1}, whereas the ν_2 PO_4^{3-} bands, typically between 430 and 550 cm^{-1} (Penel et al. 1997), are suppressed here by the broad band at 390 to 510 cm^{-1} originating from the surrounding glass.

The Raman spectra for apatite show a major band at 957 cm^{-1} associated with the ν_1 PO_4^{3-} symmetric stretching vibrations and additional lines at 1044 and 1086 cm^{-1} (ν_3 PO_4^{3-}) (Liu et al. 1998). Also, three ν_4 PO_4^{3-} vibrational bands are distinguished at 576, 586, and 607 cm^{-1}. Similar to the calciobritholite spectra, ν_2 PO_4^{3-} vibrational

bands between 430 and 550 cm^{-1} are overlapped by glass-related, high intensity broad bands at 430 to 500 cm^{-1}. Lower intensity ν_1 SiO_4^{2-} vibrational bands at 860 cm^{-1} and wide broad band 390 to 510 cm^{-1}, originating from the surrounding glass, are present in the apatite spectrum.

Discussion

Comparison with previous studies on the synthesis of britholite and high-REE apatite

The significance of the REE-bearing silico-phosphates for industrial applications and petrology have resulted in numerous studies involving the synthesis of apatite and britholite. Some studies synthesized REE silico-phosphates in relatively simple systems (e. g. Khudolozhkin et al., 1973; Terra et al., 2006). These works demonstrated the existence of these minerals as both endmember compositions as well as solid solutions (Lan et al. 2021); however, the compositions of these systems differed vastly with respect to natural melts and temperatures were typically higher than expected in natural magmas. Another set of studies focused on experiments in complex systems that consisted of mixtures of natural crystals including silicates, phosphates, and REE minerals with H_2O and reactive chemical components such as acids, alkalis, and salts (e. g. Harlov et al. 2003; Budzyn et al. 2011, 2017; Krenn et al. 2012; Betkowski et al. 2016). These experiments generated complex replacement textures that sometimes contained high-REE apatite and britholite. These studies aimed at reproducing natural metasomatic processes and typically the textures recorded incomplete reactions and anomalous compositions (Krenn et al. 2012). It has

been suggested that during the experiments, the fluid evolved to progressively to be out of equilibrium with the solid phases (Betkowski et al. 2016).

A different experimental approach has been utilized by Anenburg et al. (2020), where complex starting compositions containing carbonatite, phosphate, silicate, and REE components have been melted at 1200 °C and then gradually cooled to 200 °C. This resulted in texturally complex charges that recorded the evolution from magmatic to hydrothermal conditions and produced the mineral associations typical for REE-bearing carbonatites. Addition of silica to the carbonate-phosphate-REE system resulted in britholite overgrowing apatite. Unfortunately, the equilibrium temperature between apatite and britholite is difficult to estimate in these experiments. Molle et al. (2021) investigated the crystallisation of REE-rich carbonate and observed britholite in runs at ≥ 700 °C and apatite co-existing with britholite in one of the experiments experiment at 650 °C. Experiments that investigated the crystallization of apatite from REE-bearing melts (Watson and Green 1981; Fleet and Pan 1997; Fleet et al. 2000; Prowatke and Klemme 2006) and those that simulate melting in a subduction zone (Li and Hermann 2017) lacked britholite. Hence, the maximum REE solubility in apatite has remained unconstrained in these studies.

Previous studies have mostly achieved synthesis of britholite in simplified systems or in disequilibrium experiments. The apatite and calciobritholite reported in this study crystalized from a melt. The consistent grain size and shape of the crystals (Fig. 1) suggest uniform crystallization conditions during the experiment, implying that equilibrium has been achieved.

This is the peer-reviewed, final accepted version for American Mineralogist, published by the Mineralogical Society of America.
The published version is subject to change. Cite as Authors (Year) Title. American Mineralogist, in press.
DOI: https://doi.org/10.2138/am-2022-8535. http://www.minsocam.org/

Substitution mechanisms behind REE incorporation in apatite

REE can be incorporated into the apatite structure by several substitution mechanisms (Pan and Fleet 2002):

- $REE^{3+} + SiO_4^{4-} = Ca^{2+} + PO_4^{3-}$, referred here as the Si-REE substitution
- $REE^{3+} + Na^{+} = 2Ca^{2+}$, referred here as the Na-REE substitution
- $2REE^{3+}$ + vacancy = $3Ca^{2+}$
- $REE^{3+} + O^{2-} = Ca^{2+} + F^{-}$

The first two mechanisms likely are predominant in natural apatite (Ronsbo 1989; Pan and Fleet 2002).

The data on the substitution mechanism of REE in the natural apatite-calciobritholite-britholite series paint a complex picture (Fig. 5). The compilation by Pekov et al. (2007) reported calciobritholite analyses with a low Na content. In granites, apatite typically contains 1 to 0.5 wt.% reaching 3 wt.% TREO (Belousova et al. 2002). Apatite from mafic I-type granites preferentially contains Si-REE type substitutions, whereas apatite from S-type and felsic I-type granites mostly have a Na-REE substitution (Sha and Chappell 1999). Ronsbo (1989) observed a Si-REE substitution in magmatic apatite from sodalite foyaite and augite syenite and a Na-REE substitution in post-magmatic apatite from peralkaline pegmatite and sodalite foyaite (Fig. 5). Apatite from the carbonatite hosted Mount Weld REE deposit contains up to 3.5 wt.% TREO and is characterized by the Na-REE substitution mechanism (Zhukova et al. 2021), whereas apatite from Nolans Bore REE deposit is characterized by a Si-REE substitution (Anenburg et al. 2018).

The experiments on the equilibrium crystallisation of REE-bearing apatite from granitic to basaltic melts by Watson and Green (1981) produced apatite with a Si-REE substitution. Apatite growth from H_2O-bearing phosphate-fluoride melts

suggests (Fig. 6) that the Na-REE substitution mechanism is preferred (Fleet and Pan 1997). However, both the Na-REE and Si-REE mechanisms occurred in fluorapatite, and the Si-REE substitution dominated in hydroxyapatite (Fleet et al. 2000). Apatite with a Na+Si content significantly higher than REE has been synthesized by Prowatke and Klemme (2006) in basaltic to andesitic compositions at high temperature of 1250 °C and it was concluded that Na and Si do not control the uptake of REE. Therefore, Si-REE substitution seems to be most common in the experiments involving crystallization of apatite under equilibrium conditions from silicate melts at P-T conditions relevant for natural magmas.

Experiments on the replacement of apatite and monazite by fluid-assisted reactions in many cases have produced high-REE apatite and (calcio)britholite with both Na-REE and Si-REE substitution mechanisms (Figs. 5c, d; Fig. 6b). For example, experiment R3c by Krenn et al. (2012) at 650 °C generated apatite with both Si-REE and Na-REE substitution mechanisms (Fig. 5). Another experiment (R3d) at 800 °C produced apatite with an insignificant Si content, and 3.4 wt.% Na_2O, implying a Na-REE substitution. The apatite compositions from experiments by Budzyn et al. (2011) form two clusters with TREO < 8wt.% with TREO > 27 wt.% (Figs. 5 and 6). While the apatite had a higher Na and Si molar content than REE (Fig. 5), the britholite showed both Si-REE and Na-REE substitution mechanisms. In the synthetic system, Betkowski et al. (2016) observed britholite with an REE content close to the theoretical limit (56 – 61 wt.%TREO) in which REE substituted both via the Na-REE and Si-REE substitutions with compositions close to a line between britholite endmember and vitusite [$Na_3LREE(PO_4)_2$] (Fig. 6). The experiments by Budzyn et al. (2017) were performed with a $Ca(OH)_2$-bearing fluid generated apatite with Si-REE substitution, whereas the experiments with $Na_2Si_2O_5$-bearing fluid

315 produced apatite with both Na-REE and Si-REE substitutions (Fig. 5). Anenburg et al.
316 (2020) reported britholite and apatite with a Si-REE substitution in a Si-present, Na-
317 absent system and apatite with a Na-REE substitution in an Na-present, Si-absent
318 system.

319 The factors controlling the mechanism of REE substitution are not clear. Fleet
320 and Pan (1997) proposed that the halogen content in apatite had a significant effect on
321 REE solubility in apatite by changing the size of cation positions occupied by the
322 REE. On the other hand, Prowatke and Klemme (2006) concluded that F content had
323 limited effect. Different substitution mechanisms in apatite from granite have been
324 explained either by the preference of different substitution mechanisms to
325 LREE/HREE or the effect of Al in peraluminous granites (Sha and Chappell 1999).
326 The fluid composition was proposed to play a major role during the metasomatic
327 reactions (Krenn et al. 2012; Betkowski et al. 2016; Budzyn et al. 2017).

328 In this study, apatite and calciobritholite, crystallized from a high-Na melt, had
329 an insignificant Na content (Table 1). The Raman spectra (Fig. 4) show that the SiO_4^{4-}
330 related vibration bands provide additional evidence for Si-REE substitution in the
331 apatite. Most reported natural britholite compositions have a negligible Na content
332 such that the Si-REE mechanism predominats (Fig. 6), which implies that the Si-REE
333 substitution could be characteristic for magmatic apatite-britholite. It could be further
334 speculated, that the Na-REE substitution is characteristic for post-magmatic, fluid-
335 aided recrystallisation. This is evident from observations of the experimental
336 decomposition of fluorapatite with significant britholite and fluorellestadite
337 components that resulted in the formation of Na-REE substituted apatite (Harlov et al.
338 2003). In agreement with this hypothesis, crystallisation of apatite with the Si-REE
339 substitution has been observed in magmatic apatite from the Ilimaussaq complex,

Greenland, while the Na-REE substitution has been observed in metasomatically altered apatite (Zirner et al. 2015). Additional studies are needed to clarify the factors controlling the substitution mechanism of REE in apatite. In that regard caution is needed when the REE substitution type in apatite is used for the genetic interpretations as proposed by Ronsbo (1989).

Miscibility gap between apatite and britholite

Several studies have proposed that there is complete miscibility between apatite and britholite at high temperature, and a miscibility gap at lower temperature (Anenburg et al. 2018; Lorenz et al. 2019), although the exact position of the miscibility gap is poorly constrained. We have used past experimental data and the results from this work to obtain new constraints on the position of the miscibility gap (Fig. 7). Complete solid solutions between fluorapatite and britholite have been observed between 1200 to 1400 °C (Boyer et al. 1997).

A study of the phase relations in the system CaO-SiO_2-CaF_2-P_2O_5-Ce_2O_3 by Lan et al. (2021) demonstrated a complete solid solution between apatite and britholite at 1100 °C. The composition ranged from fluorapatite with 8.8 % Si/(Si+P) to britholite with 70.1 % Si/(Si+P) and 70.9 wt.% Ce_2O_3. Attempts by Terra et al. (2006) to synthesize Th-bearing britholite with formula $Ca_9Nd_{1-x}Th_x(PO_4)_{5-x}(SiO_4)_{1+x}F_2$ at temperatures below 1000 °C produced apatite co-existing with Nd_2O_3 and ThO_2, which was explained as being due to a slow reaction rate. Watson and Green (1981) synthesized apatite from granitic melts with up to 21.2 wt.% TREO at 950 °C. Apatite with up to 7.8 wt.% TREO have been observed at 680 °C by Fleet and Pan (1997). Chlorapatite with 1 to 2 wt.% TREO coexisting with allanite and melt was synthesized at 800 °C in metasediments by Li and Hermann (2017). Data from all

365 of these experiments on equilibrium crystallization of high-REE apatite and/or
366 britholite show that the range of conditions where the immiscibility could disappear is
367 limited and should be about 950 °C (Fig. 7).

368 Many compositions from the metasomatism experiments involving fluids plot
369 within the miscibility gap estimated from the melt crystallization experiments (Fig.
370 7b). The elevated REE contents of the replacement textures observed in the
371 metasomatized apatite could be attributed to the development of temporary
372 disequilibrium products during the evolution of these textures, i.e. metastability (Borg
373 et al. 2014; Altree-Williams et al. 2015). Notably, with a decrease in temperature, the
374 gap between apatite and britholite becomes narrower with the narrowest gap
375 apparently occurring at 450 °C (Fig. 7b). This is similar to what is seen for metastable
376 arsenian pyrite (Stepanov et al. 2021), where a widening in the range of compositions
377 at lower temperature could be attributed to a slowdown in the rate diffusion with
378 decreasing temperature (Watson 2004).
379

380 **Effect of NaCl on accessory mineral assemblages and solubility**

381 The addition of NaCl to the REE-enriched granitic melt resulted in the
382 crystallization of co-existing calciobritholite and apatite, which is in marked contrast
383 to the crystallisation of monazite for the same system under identical conditions,
384 though without NaCl (Stepanov et al. 2012). The addition of NaCl affected the melt
385 composition twofold by adding Cl and increasing the Na content of the melt, which
386 led to an increase in alkalinity (Table 1). Monazite can crystallize in alkaline,
387 halogen-free melts (Fig. 3); hence, the alkalinity of the melt was not a major factor in
388 controlling the accessory mineral assemblage. More likely, it appears that the high Cl

389 content in the melt helped to stabilize apatite and calciobritholite at the expense of
390 monazite.

391 The solubility of Cl in melts is a complex function of melt composition
392 (Webster and Vivo 2002) and the immiscible chloride melts that can coexist with
393 felsic melts (Veksler et al. 2012). The 0.51 wt.% Cl measured in the glass is close to
394 the 0.39 wt.% Cl observed in granitic melts coexisting with chloride melts at 800 °C
395 in the experiments by Veksler et al. (2012), and is within the range of 0.14–0.9 wt.%
396 Cl that has been reported in Cl-saturated granitic to alkaline melts (Webster and Vivo
397 2002).

398 The P content of 112 ± 49 ppm in the glass obtained in this study (Table 1) is
399 significantly lower than the 311 ± 30 ppm P in experiment C4025 from the study of
400 Stepanov et al. (2012), which was performed under identical P-T conditions and
401 contained only abundant monazite and melt. While the crystallization of REE-
402 minerals with the addition of NaCl decreased the P content in the glass, the LREE
403 content increased from 292 ± 15 ppm Ce in the glass from the monazite buffered
404 experiment C4025 (Table 4 at Stepanov et al. (2012)) to 526 ± 19 ppm Ce in the glass
405 from the apatite-calciobritholite buffered melt (Table 1). Crystallisation of apatite and
406 calciobritholite caused an increase of LREE/P in the melt relative to the monazite-
407 saturated experiments. Li and Hermann (2017) observed 718 to 1064 ppm P at 25
408 kbar and 800 °C in apatite buffered metasediment-derived melts. Watson and
409 Capobianco (1981) performed experiments with a variable CaF_2 component and
410 observed the lowest P concentrations in melts with the highest F content (Fig. 3).
411 These results suggest that a high halogen content in the melt can alter the accessory
412 mineral assemblage and melt trace element composition by stabilizing apatite and
413 calcobritholite. This conclusion could be at odds with Duc-Tin and Keppler (2015)

414 and Van Lichtervelde et al. (2021), who observed crystallization of monazite and
415 xenotime from melts with significant amounts of F. However, those experiments were
416 performed in Ca-free or low-Ca melts unfavorable to apatite crystallisation. These
417 observations suggest that Ca and halogens are important in the modelling and
418 interpretation of accessory mineral associations.
419

420 **Partitioning of trace elements**

421 Application of partition coefficients in petrology is based on the Henry's law
422 behaviour, namely a change in the trace element content in a melt results in a direct
423 proportional change in the element's content in the mineral (Drake and Holloway
424 1981). Studies have shown that for accessory phases, some factors can affect the
425 applicability of Henry's law (Prowatke and Klemme 2005). For REE in apatite, the
426 validity of Henry's law has been tested by Watson and Green (1981) in a set of
427 experiments with varying REE content of REE in the system from 0.4 to 3.2 wt.%
428 TREO. These experiments demonstrated that REE partition coefficients were
429 independent of concentration. The situation recorded by the experiment in this study
430 is different (Fig. 8). The presence of two REE-bearing phases implies that the melt
431 composition likely was buffered with respect to the REE. Any addition of REE to the
432 system would have resulted in the crystallisation of a surplus amount of
433 calciobritholite and high-REE apatite with little effect on the REE content in the melt.
434 For individual REE, the situation is likely different. The REE partition pattern
435 for apatite and calciobritholite is smooth and similar to other experimental data on
436 apatite-melt partitioning despite non-chondritic ratios of some REE in the starting
437 composition (Fig. 8). The negative Eu anomaly, which results from the relatively
438 reduced conditions, during the piston-cylinder experiment, is the same for both apatite

and calciobritholite. Therefore, while Henry's law was unlikely to act on the total REE content, it is still possible to use the composition of calciobritholite and high-REE apatite to predict the distribution pattern of REE patterns for melts coexisting with these minerals.

The partitioning of REE between apatite and melt has been explored in several studies (Fleet et al. 2000; Prowatke and Klemme 2006; Li and Hermann 2017). Our data and previous studies consistently show the preference of apatite and calciobritholite for MREE relative to LREE and HREE (Fig. 8). However, the REE partition coefficients could be sensitive to the melt composition (Watson and Green 1981; Prowatke and Klemme 2006) and the anionic composition of the apatite (Fleet et al. 2000; Li and Hermann 2017). Watson and Green (1981) observed that REE compatibility in apatite increased with increasing silica activity. This effect can be attributed to the stabilization of the Si-REE substitution mechanism in apatite due to the presence of felsic melts.

Li and Hermann (2017) demonstrated that Th and U in apatite were positively correlated with the apatite Cl content. This observation agrees with our results, where the Cl-rich apatite contains as much as 1 wt.% of Th (Table 1). A high D_{Th} for calciobritholite could explain the very high Th content of 13-15 wt.% ThO_2 observed in some localities (Pekov et al. 2007).

Implications: Interpretation of natural (calcio)britholite-bearing associations

Intrusive alkaline rocks and associated REE deposits sometimes show complex symplectites of apatite, britholite, monazite, and other REE minerals (Anenburg et al. 2018; Lorenz et al. 2019). The results from this study have implications for the interpretation of these textures.

464 The compositions of apatite-britholite in trachytes from the Phlegrean Fields
465 volcanic system in Italy (Melluso et al. 2012) show a wide range of compositions,
466 including compositions within the miscibility gap proposed in this study (Figs. 5, 7).
467 These variations could be attributed to the different temperatures during the
468 crystallisation of these minerals. Samples with compositions in the proposed
469 miscibility gap likely crystallized above 950 °C. The preservation of high-temperature
470 compositions could be attributed to the rapid cooling of the volcanic rocks.
471 Complex fluorapatite and britholite textures have been observed in the Misery
472 syenitic intrusion, Canada (Petrella et al. 2014). Apatite containing about 10.7 wt.%
473 TREO makes up the cores of the zoned crystals, whereas britholite with 32 to 43 wt.%
474 TREO was observed in the rims. These textures can be explained by crystallisation at
475 temperatures within the miscibility gap.
476 Symplectites of apatite and britholite have been described in the Rodeo de los
477 Molles deposit, Argentina (Lorenz et al. 2019). The symplectites can be divided into
478 two types: fluorapatite-hosted with britholite inclusions and britholite-hosted with
479 fluorapatite inclusions (their Supplemental Figure S1). Tentatively, the fluorapatite
480 with britholite inclusions could be interpreted as a product of
481 decomposition/exsolution of high temperature, high-REE apatite, whereas britholite
482 with apatite inclusions could have originated as a high-temperature britholite-apatite
483 solid solution above the miscibility gap. Therefore, the textures of the Rodeo de los
484 Molles deposit could indicate crystallization at conditions close to the complete solid
485 solution between apatite and britholite, which was then followed by unmixing and
486 recrystallisation at lower temperatures.
487 The potential of REE in apatite as a geothermometer requires some discussion.
488 The application of such a geothermometer would first require characterization of

489 factors controlling substitution mechanisms for the REE in apatite and, ideally,
490 experiments involving apatite coexisting with REE minerals in as simple a system as
491 possible, which was buffered with respect to the elements involved.
492

493 **Acknowledgement**

494 Centre for advanced microscopy and Frank Brink are thanked for help with
495 SEM and EDS investigation. Terry Mernagh is thanked for help with the collection of
496 Raman spectra. Joerg Hermann and Daniela Rubatto are thanked for providing
497 research facilities. Michael Anenburg and Melanie Lorenz are thanked for
498 constructive reviews and Daniel Harlov for editorial handling. This study was
499 supported by the grants No. 40030811, 42073058 and 42073036 of the National
500 Natural Science Foundation of China, and 100 Talents of Hubei Province Program.
501

502 **Figures and tables**

503

504 **Figure 1: a**) SEM image of the experimental texture showing NaCl crystals formed
505 along the cracks in the glass. **b**) BSE image of the elongated crystals of
506 calciobritholite and apatite in the glass. Small vapor bubbles formed in the glass
507 during quenching.
508

509 **Figure 2:** Examples of regression of LA-ICP-MS data obtained by the segmentation
510 of time resolved spectra.
511

512 **Figure 3:** Comparison of the REE (**a**) and P content (**b**) in the melts from this study
513 with melts saturated in monazite or apatite.
514
515 **Figure 4:** Raman spectra of the experimental apatite and britholite phases compared
516 with apatite and britholite from the RRUFF database (Lafuente et al. 2015).
517
518 **Figure 5:** Binary plots of britholite and apatite compositions from natural occurrences
519 (**a**, **b**) and experiments (**c**, **d**). Compositions are shown in atoms per formula unit
520 normalized to 16 cations.
521
522 **Figure 6:** Ternary Na-Ca-REE plots showing the different substitution mechanism for
523 REE in apatite and britholite from natural samples (**a**) and from experimental data (**b**).
524
525 **Figure 7:** A summary of experimental data on the effect of temperature on the REE
526 content of apatite and britholite.
527
528 **Figure 8: a**) Partition coefficients between calciobritholite, apatite, and melt in
529 comparison with the apatite partition data of Li and Hermann (2017). **b**) Partition
530 patterns of apatite, calciobritholite, and monazite from Stepanov et al. (2012)
531 normalized to unity for D_{Dy} and highlight differences in the fractionation of the
532 lanthanides and actinides.
533
534
535

References

Altree-Williams, A., Pring, A., Ngothai, Y., and Brugger, J. (2015) Textural and compositional complexities resulting from coupled dissolution–reprecipitation reactions in geomaterials. Earth-Science Reviews, 150, 628–651.

Anenburg, M., Burnham, A.D., and Mavrogenes, J.A. (2018) REE Redistribution Textures in Altered Fluorapatite: Symplectites, Veins, and Phosphate-Silicate-Carbonate Assemblages from the Nolans Bore P-REE-Th Deposit, Northern Territory, AustraliaRee in Altered Fluorapatites: Symplectites, Veins, and P-si-c Assemblages. The Canadian Mineralogist, 56, 331–354.

Anenburg, M., Mavrogenes, J.A., Frigo, C., and Wall, F. (2020) Rare earth element mobility in and around carbonatites controlled by sodium, potassium, and silica. Science Advances, 6, eabb6570.

Belousova, E.A., Griffin, W.L., O'Reilly, S.Y., and Fisher, N.I. (2002) Apatite as an indicator mineral for mineral exploration: trace-element compositions and their relationship to host rock type. Journal of Geochemical Exploration, 76, 45–69.

Betkowski, W.B., Harlov, D.E., and Rakovan, J.F. (2016) Hydrothermal mineral replacement reactions for an apatite-monazite assemblage in alkali-rich fluids at 300–600 °C and 100 MPa. American Mineralogist, 101, 2620–2637.

Borg, S., Liu, W., Pearce, M., Cleverley, J., and MacRae, C. (2014) Complex mineral zoning patterns caused by ultra-local equilibrium at reaction interfaces. Geology, 42, 415–418.

Boyer, L., Carpena, J., and Lacout, J.L. (1997) Synthesis of phosphate-silicate apatites at atmospheric pressure. Solid State Ionics, 95, 121–129.

Budzyn, B., Harlov, D.E., Williams, M.L., and Jercinovic, M.J. (2011) Experimental determination of stability relations between monazite, fluorapatite, allanite, and ree-epidote as a function of pressure, temperature, and fluid composition. American Mineralogist, 96, 1547–1567.

Budzyn, B., Harlov, D.E., Kozub-Budzyń, G.A., and Majka, J. (2017) Experimental constraints on the relative stabilities of the two systems monazite-(Ce) – allanite-(Ce) – fluorapatite and xenotime-(Y) – (Y,HREE)-rich epidote – (Y,HREE)-rich fluorapatite, in high Ca and Na-Ca environments under P-T conditions of 200–1000 MPa and 450–750 °C. Mineralogy and Petrology, 111, 183–217.

Bussweiler, Y., Gervasoni, F., Rittner, M., Berndt, J., and Klemme, S. (2020) Trace element mapping of high-pressure, high-temperature experimental samples with laser ablation ICP time-of-flight mass spectrometry – Illuminating melt-rock reactions in the lithospheric mantle. Lithos, 352–353, 105282.

Chakhmouradian, A.R., Reguir, E.P., Zaitsev, A.N., Couëslan, C., Xu, C., Kynický, J., Mumin, A.H., and Yang, P. (2017) Apatite in carbonatitic rocks:

576 Compositional variation, zoning, element partitioning and petrogenetic
577 significance. Lithos, 274–275, 188–213.

578 Drake, M.J., and Holloway, J.R. (1981) Partitioning of Ni between olivine and silicate
579 melt: The 'Henry's Law problem' reexamined. Geochimica et Cosmochimica
580 Acta, 45, 431–437.

581 Duc-Tin, Q., and Keppler, H. (2015) Monazite and xenotime solubility in granitic
582 melts and the origin of the lanthanide tetrad effect. Contributions to
583 Mineralogy and Petrology, 169, 1–26.

584 Fleet, M., Liu, X., and Pan, Y. (2000) Rare-earth elements in chlorapatite [Ca-
585 10(PO4)(6)Cl-2]: Uptake, site preference, and degradation of monoclinic
586 structure. American Mineralogist, 85, 1437–1446.

587 Fleet, M.E., and Pan, Y. (1997) Rare earth elements in apatite: Uptake from H2O-
588 bearing phosphate-fluoride melts and the role of volatile components.
589 Geochimica et Cosmochimica Acta, 61, 4745–4760.

590 Goldoff, B., Webster, J.D., and Harlov, D.E. (2012) Characterization of fluor-
591 chlorapatites by electron probe microanalysis with a focus on time-dependent
592 intensity variation of halogens. American Mineralogist, 97, 1103–1115.

593 Harlov, D.E., Förster, H.-J., and Schmidt, C. (2003) High P-T experimental
594 metasomatism of a fluorapatite with significant britholite and fluorellestadite
595 components: implications for LREE mobility during granulite-facies
596 metamorphism. Mineralogical Magazine, 67, 61–72.

597 Janots, E. (2008) Thermochemical characterization of ca4la6(sio 4)6(oh)2 a synthetic
598 la- and oh-analogous of britholite: implication for monazite and lree apatites
599 stability. Mineralogia, 39, 41–52.

600 Jochum, K.P., Weis, U., Stoll, B., Kuzmin, D., Yang, Q., Raczek, I., Jacob, D.E.,
601 Stracke, A., Birbaum, K., Frick, D.A., and others (2011) Determination of
602 Reference Values for NIST SRM 610–617 Glasses Following ISO Guidelines.
603 Geostandards and Geoanalytical Research, 35, 397–429.

604 Khudolozhkin, V., Urusov, V.S., Tobelko, K., and Vernadskiy, V. (1973) Dependence
605 of structural ordering of rare earth atoms in the isomorphous series apatite-
606 britholite (abukumalite) on composition and temperature. Geochemistry
607 International, 10, 1171–1177.

608 Krenn, E., Harlov, D.E., Finger, F., and Wunder, B. (2012) LREE-redistribution
609 among fluorapatite, monazite, and allanite at high pressures and temperatures.
610 American Mineralogist, 97, 1881–1890.

611 Lafuente, B., Downs, R.T., Yang, H., and Stone, N. (2015) 1. The power of databases:
612 The RRUFF project. In 1. The power of databases: The RRUFF project pp. 1–
613 30. De Gruyter (O).

614 Lan, X., Gao, J., Li, Y., and Guo, Z. (2021) Phase equilibria of CaO–SiO2–CaF2–
615 P2O5–Ce2O3 system and formation mechanism of britholite. Ceramics
616 International, 47, 11966–11972.

617 Le Maitre, R.W., Streckeisen, A., Zanettin, B., Le Bas, M.J., Bonin, B., and Bateman,
618 P., Eds. (2002) Igneous Rocks: A Classification and Glossary of Terms:
619 Recommendations of the International Union of Geological Sciences
620 Subcommission on the Systematics of Igneous Rocks, 2nd ed. Cambridge
621 University Press, Cambridge.

622 Li, H., and Hermann, J. (2017) The effect of fluorine and chlorine on trace element
623 partitioning between apatite and sediment melt at subduction zone conditions.
624 Chemical Geology, 473, 55–73.

625 Liu, Y., Comodi, P., and Sassi, P. (1998) Vibrational Spectroscopic Investigation of
626 Phosphate Tetrahedron in Fluor-, Hydroxy-, and Chlorapatites. Neues
627 Jahrbuch für Mineralogie - Abhandlungen, 211–222.

628 Lorenz, M., Altenberger, U., Trumbull, R.B., Lira, R., Luchi, M.L. de, Günter, C., and
629 Eidner, S. (2019) Chemical and textural relations of britholite- and apatite-
630 group minerals from hydrothermal REE mineralization at the Rodeo de los
631 Molles deposit, Central Argentina. American Mineralogist, 104, 1840–1850.

632 Melluso, L., Gennaro, R.D., Fedele, L., Franciosi, L., and Morra, V. (2012) Evidence
633 of crystallization in residual, Cl–F-rich, agpaitic, trachyphonolitic magmas and
634 primitive Mg-rich basalt–trachyphonolite interaction in the lava domes of the
635 Phlegrean Fields (Italy). Geological Magazine, 149, 532–550.

636 Molle, V., Gaillard, F., Nabyl, Z., Tuduri, J., Carlo, I.D., and Erdmann, S. (2021)
637 Crystallisation sequence of a REE-rich carbonate melt: an experimental
638 approach. Comptes Rendus. Géoscience, 353, 217–231.

639 Nikolenko, A.M., Redina, A.A., Doroshkevich, A.G., Prokopyev, I.R., Ragozin, A.L.,
640 and Vladykin, N.V. (2018) The origin of magnetite-apatite rocks of Mushgai-
641 Khudag Complex, South Mongolia: mineral chemistry and studies of melt and
642 fluid inclusions. Lithos, 320–321, 567–582.

643 O'Sullivan, G., Chew, D., Kenny, G., Henrichs, I., and Mulligan, D. (2020) The trace
644 element composition of apatite and its application to detrital provenance
645 studies. Earth-Science Reviews, 201, 103044.

646 Pan, Y., and Fleet, M.E. (2002) Compositions of the Apatite-Group Minerals:
647 Substitution Mechanisms and Controlling Factors. Reviews in Mineralogy and
648 Geochemistry, 48, 13–49.

649 Pekov, I.V., Pasero, M., Yaskovskaya, A.N., Chukanov, N.V., Pushcharovsky, D.Y.
650 u, Merlino, S., Zubkova, N.V., Kononkova, N.N., Men'shikov, Y.P., and
651 Zadov, A.E. (2007) Fluorcalciobritholite, (Ca,REE)5[(Si,P)O4]3F, a new
652 mineral: description and crystal chemistry. European Journal of Mineralogy,
653 95–103.

Penel, G., Leroy, G., Rey, C., Sombret, B., Huvenne, J.P., and Bres, E. (1997) Infrared and Raman microspectrometry study of fluor-fluor-hydroxy and hydroxy-apatite powders. Journal of Materials Science: Materials in Medicine, 8, 271–276.

Petrella, L., Williams-Jones, A.E., Goutier, J., and Walsh, J. (2014) The Nature and Origin of the Rare Earth Element Mineralization in the Misery Syenitic Intrusion, Northern Quebec, Canada. Economic Geology, 109, 1643–1666.

Prowatke, S., and Klemme, S. (2005) Effect of melt composition on the partitioning of trace elements between titanite and silicate melt. Geochimica et Cosmochimica Acta, 69, 695–709.

Prowatke, S., and Klemme, S. (2006) Trace element partitioning between apatite and silicate melts. Geochimica et Cosmochimica Acta, 70, 4513–4527.

Ronsbo, J.G. (1989) Coupled substitutions involving REEs and Na and Si in apatites in alkaline rocks from the Ilimaussaq Intrusion, South Greenland, and the petrological implications. American Mineralogist, 74, 896–901.

Rubatto, D., and Hermann, J. (2007) Experimental zircon/melt and zircon/garnet trace element partitioning and implications for the geochronology of crustal rocks. Chemical Geology, 241, 38–61.

Sha, L.-K., and Chappell, B.W. (1999) Apatite chemical composition, determined by electron microprobe and laser-ablation inductively coupled plasma mass spectrometry, as a probe into granite petrogenesis. Geochimica et Cosmochimica Acta, 63, 3861–3881.

Stepanov, A.S., Hermann, J., Rubatto, D., and Rapp, R.P. (2012) Experimental study of monazite/melt partitioning with implications for the REE, Th and U geochemistry of crustal rocks. Chemical Geology, 300–301, 200–220.

Stepanov, A.S., Danyushevsky, L.V., Large, R.R., Mukherjee, I., and Zhukova, I.A. (2020) Deconvolution of the composition of fine-grained pyrite in sedimentary matrix by regression of time-resolved LA-ICP-MS data. American Mineralogist, 105, 820–832.

Stepanov, A.S., Large, R.R., Kiseeva, E.S., Danyushevsky, L.V., Goemann, K., Meffre, S., Zhukova, I., and Belousov, I.A. (2021) Phase relations of arsenian pyrite and arsenopyrite. Ore Geology Reviews, 136, 104285.

Stock, M.J., Humphreys, M.C.S., Smith, V.C., Johnson, R.D., Pyle, D.M., and EIMF (2015) New constraints on electron-beam induced halogen migration in apatite†. American Mineralogist, 100, 281–293.

Stormer, J.C., Pierson, M.L., and Tacker, R.C. (1993) Variation of F and Cl X-ray intensity due to anisotropic diffusion in apatite during electron microprobe analysis. American Mineralogist, 78, 641–648.

692 Terra, O., Audubert, F., Dacheux, N., Guy, C., and Podor, R. (2006) Synthesis and
693 characterization of thorium-bearing britholites. Journal of Nuclear Materials,
694 354, 49–65.

695 Van Lichtervelde, M., Goncalves, P., Eglinger, A., Colin, A., Montel, J.-M., and
696 Dacheux, N. (2021) Solubility of Monazite-Cheralite and Xenotime in
697 Granitic Melts, and Experimental Evidence of Liquid-Liquid Immiscibility in
698 Concentrating REE. Journal of Petrology.

699 Veksler, I.V., Dorfman, A.M., Dulski, P., Kamenetsky, V.S., Danyushevsky, L.V.,
700 Jeffries, T., and Dingwell, D.B. (2012) Partitioning of elements between
701 silicate melt and immiscible fluoride, chloride, carbonate, phosphate and
702 sulfate melts, with implications to the origin of natrocarbonatite. Geochimica
703 et Cosmochimica Acta, 79, 20–40.

704 Watson, E.B. (2004) A conceptual model for near-surface kinetic controls on the
705 trace-element and stable isotope composition of abiogenic calcite crystals1.
706 Geochimica et Cosmochimica Acta, 68, 1473–1488.

707 Watson, E.B., and Capobianco, C.J. (1981) Phosphorus and the rare earth elements in
708 felsic magmas: an assessment of the role of apatite. Geochimica et
709 Cosmochimica Acta, 45, 2349–2358.

710 Watson, E.B., and Green, T.H. (1981) Apatite/liquid partition coefficients for the rare
711 earth elements and strontium. Earth and Planetary Science Letters, 56, 405–
712 421.

713 Webster, J.D., and Vivo, B.D. (2002) Experimental and modeled solubilities of
714 chlorine in aluminosilicate melts, consequences of magma evolution, and
715 implications for exsolution of hydrous chloride melt at Mt. Somma-Vesuvius.
716 American Mineralogist, 87, 1046–1061.

717 Yudovich, Ya.E., Ketris, M.P., and Rybina, N.V. (2022) The apatite-deceiver as an
718 unique indicator parent rocks and ores, as well as petro-, litho- and ore
719 genesis.

720 Zhukova, I.A., Stepanov, A.S., Jiang, S.-Y., Murphy, D., Mavrogenes, J., Allen, C.,
721 Chen, W., and Bottrill, R. (2021) Complex REE systematics of carbonatites
722 and weathering products from uniquely rich Mount Weld REE deposit,
723 Western Australia. Ore Geology Reviews, 139, 104539.

724 Zirner, A.L.K., Marks, M.A.W., Wenzel, T., Jacob, D.E., and Markl, G. (2015) Rare
725 earth elements in apatite as a monitor of magmatic and metasomatic processes:
726 The Ilímaussaq complex, South Greenland. Lithos, 228–229, 12–22.

727

728

729

Table 1. Compositions of experimental phases and estimated partition coefficients.

	Melt	*sd*	Apatite	*sd*		Calciobritholite	*sd*	
n	4	sd	4	sd		4	sd	
SiO_2, wt%	64.8	0.20	2.9	1.3		10.0	2.0	
Al_2O_3	12.9	0.12	<0.1			<0.1		
CaO	2.0	0.09	46.4	3.0		29.1	6.5	
Na_2O	5.2	0.06	<0.1			<0.1		
K_2O	2.9	0.04	<0.1			<0.1		
P_2O_5	na		34.3	3.2		19.4	4.7	
La_2O_3	na		2.5	0.7		7.6	1.4	
Ce_2O_3	na		5.0	1.4		15.0	2.6	
Nd_2O_3	na		2.8	0.9		6.6	0.5	
ThO_2	na		1.0	0.2		4.6	1.3	
Cl	0.51	0.02	1.1	0.2		1.2	0.2	
H_2O*	11.6							
Total	88.4		98.8			101.6		
	Melt		Apatite	*sd*	D Ap/melt	Calciobritholite	*sd*	D Cbrt/melt
P, ppm	112	49	138695	416		74471	385	
Sr	23.4	1.2	68	1.9	2.9	88	2.56	3.7
Y	88.9	4.4	9112	27.6	103	17506	50.8	197
Ba	14.0	1.5	11	3.2	0.8	18	3.6	1.3
Zr	198	10.5	42	17.5	0	381	17.3	2
La	336	15.8	19561	26	58	60334	79	180
Ce	526	19.3	43000	11591	82	128000	22273	243
Pr	53	2.3	5480	7	104	16101	20	304
Nd	168	10.1	23037	29	137	63206	84	377
Sm	28	1.6	4485	8	160	11121	24	398
Eu	10	0.8	1109	3	108	2655	6	259
Gd	20	2.1	3711	12	183	8229	21	406
Tb	5.5	0.6	883	2	160	1824	4	331
Dy	20	1.5	2695	8	137	5479	13	279
Ho	6.8	0.6	860	2	127	1722	4	254
Er	7.4	0.7	743	2	101	1464	3	199
Tm	8.2	0.7	690	3	85	1254	3	154
Yb	9.1	1.2	550	3	60	1068	4	117
Lu	9.4	0.5	462	2	49	940	3	100
Pb	1.5	0.7	29	1	19	26	2	17
Th	155	8.4	9327	18	60	38216	110	247
U	12	1.0	881	2	74	2088	7	175

*H_2O estimated from the total deficit.

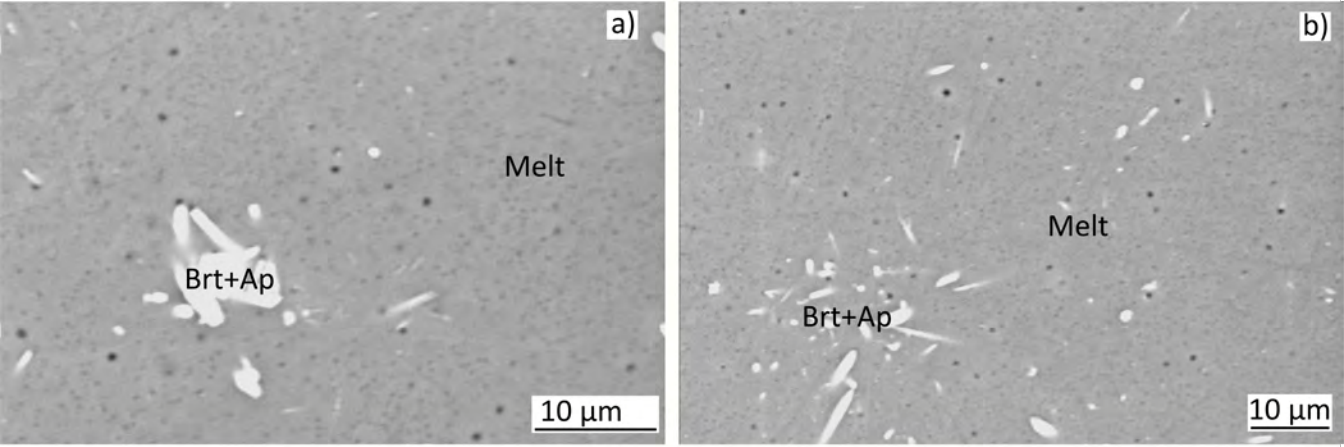

Figure 1

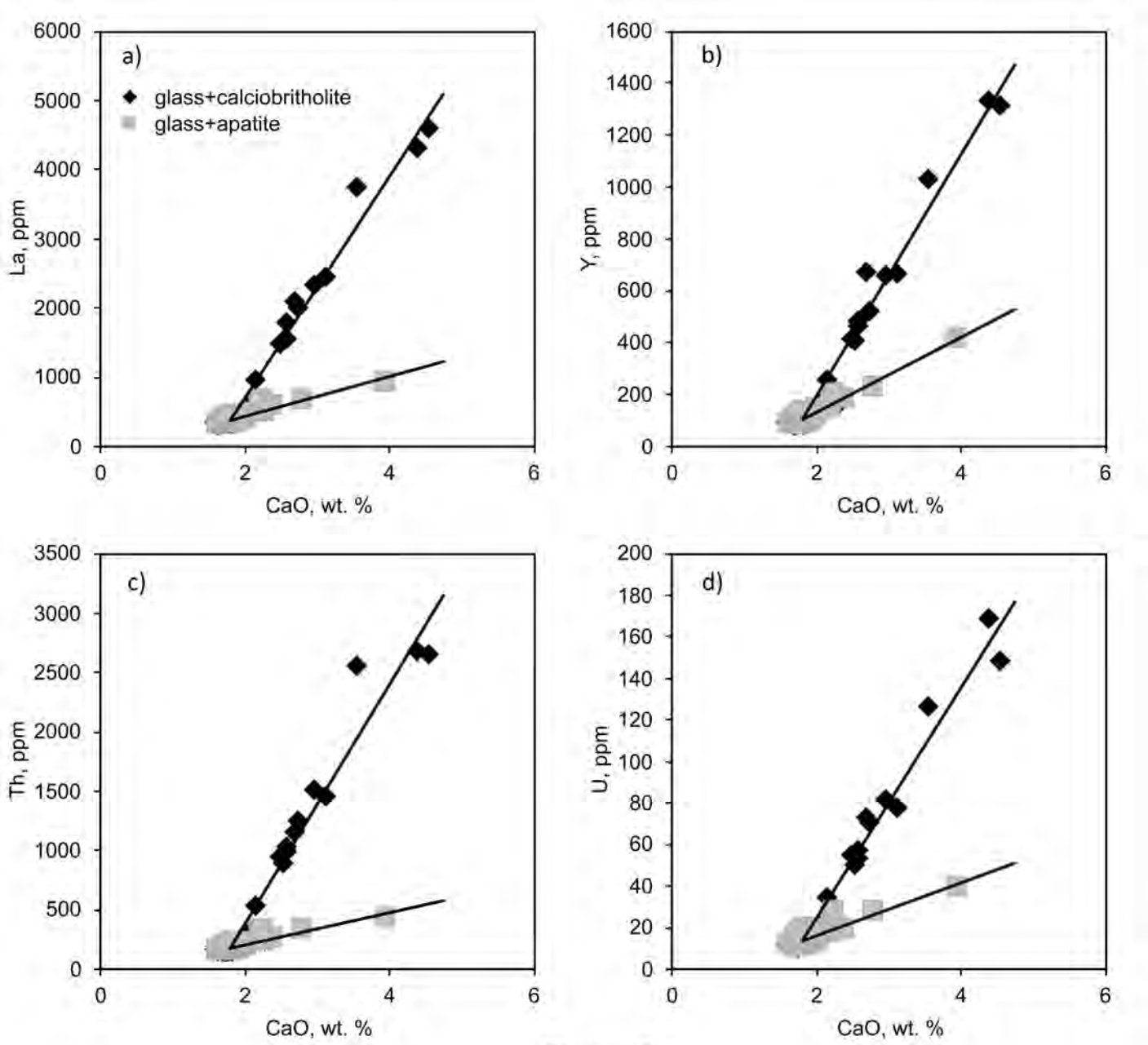
a)
glass+calciobritholite
glass+apatite
La, ppm
CaO, wt. %
b)
Y, ppm
CaO, wt. %
c)
Th, ppm
CaO, wt. %
d)
U, ppm
CaO, wt. %

Figure 2

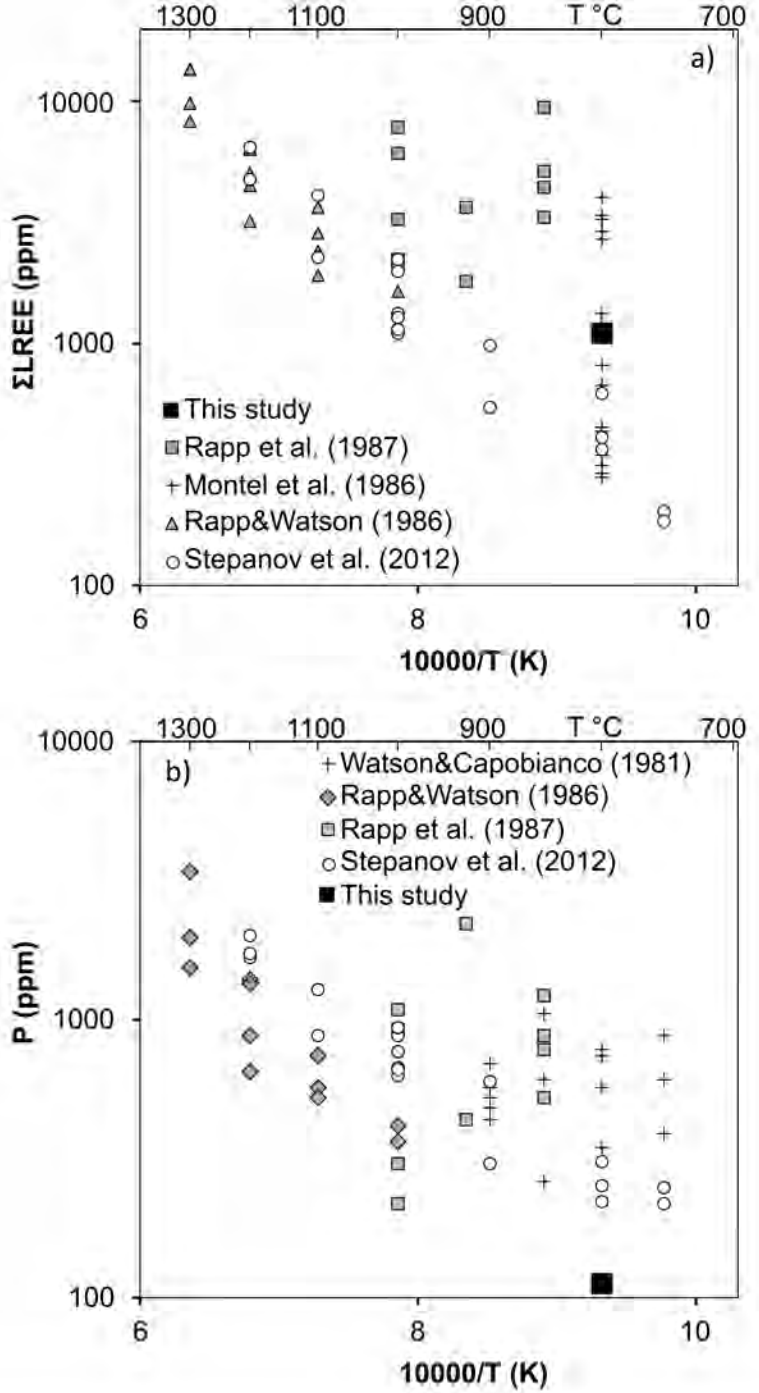
1300
1100
900
T °C
700
a)
10000
1000
100
ΣLREE (ppm)
This study
Rapp et al. (1987)
Montel et al. (1986)
Rapp&Watson (1986)
Stepanov et al. (2012)
6
8
10
10000/T (K)
1300
1100
900
T °C
700
10000
b)
Watson&Capobianco (1981)
Rapp&Watson (1986)
Rapp et al. (1987)
Stepanov et al. (2012)
This study
P (ppm)
1000
100
6
8
10
10000/T (K)

Figure 3

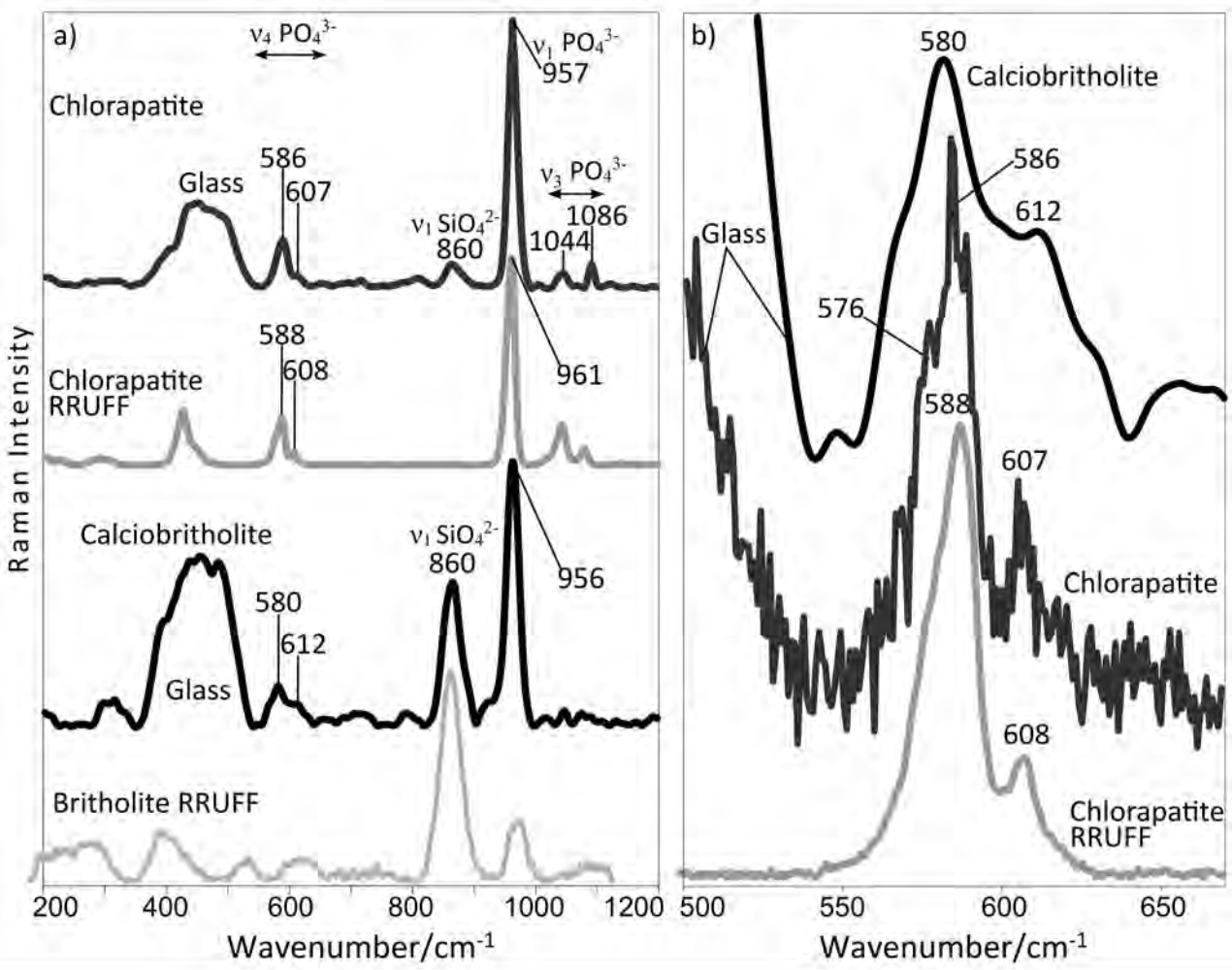
a)
ν_4 PO_4^{3-}
ν_1 PO_4^{3-}
957
Chlorapatite
Glass
586
607
ν_3 PO_4^{3-}
1086
ν_1 SiO_4^{2-}
860
1044
588
608
961
Chlorapatite
RRUFF
Calciobritholite
ν_1 SiO_4^{2-}
860
956
580
612
Glass
Britholite RRUFF
Raman Intensity
200
400
600
800
1000
1200
Wavenumber/cm^{-1}
b)
580
Calciobritholite
586
612
Glass
576
588
607
Chlorapatite
608
Chlorapatite
RRUFF
500
550
600
650
Wavenumber/cm^{-1}

Figure 4

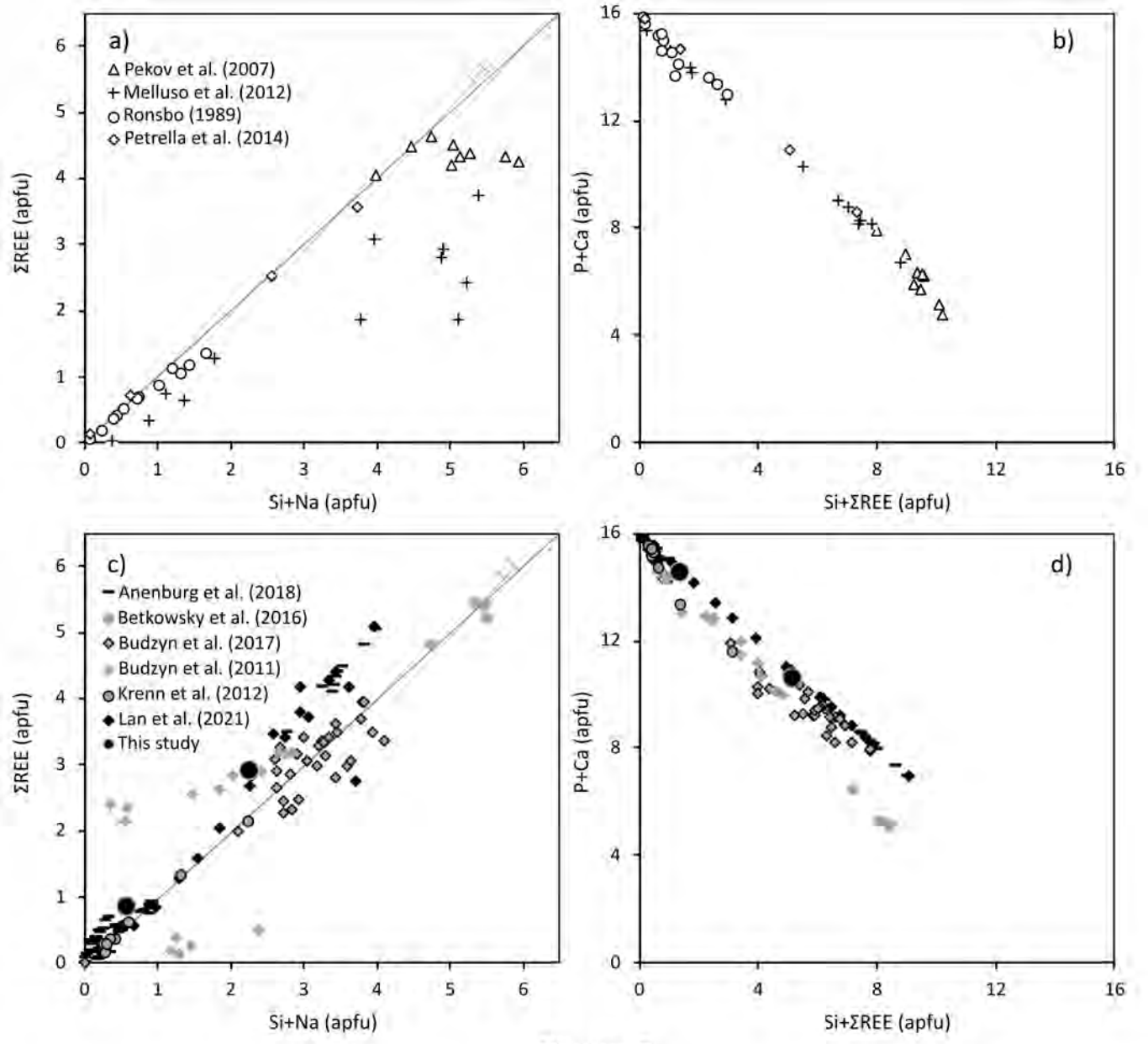
a)
Pekov et al. (2007)
Melluso et al. (2012)
Ronsbo (1989)
Petrella et al. (2014)
ΣREE (apfu)
Si+Na (apfu)
b)
P+Ca (apfu)
Si+ΣREE (apfu)
c)
Anenburg et al. (2018)
Betkowsky et al. (2016)
Budzyn et al. (2017)
Budzyn et al. (2011)
Krenn et al. (2012)
Lan et al. (2021)
This study
ΣREE (apfu)
Si+Na (apfu)
d)
P+Ca (apfu)
Si+ΣREE (apfu)

Figure 5

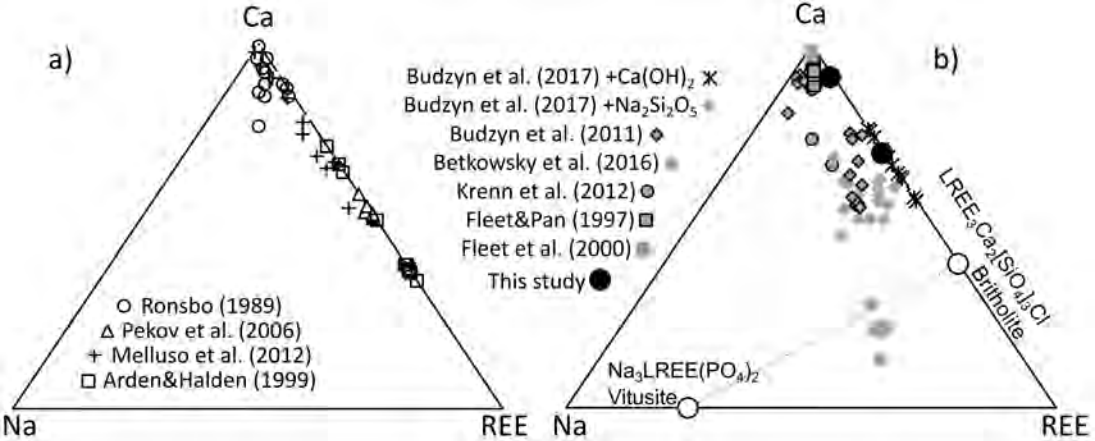
Ca
a)
Budzyn et al. (2017) +Ca(OH)2
Budzyn et al. (2017) +Na2Si2O5
Budzyn et al. (2011)
Betkowsky et al. (2016)
Krenn et al. (2012)
Fleet&Pan (1997)
Fleet et al. (2000)
This study
Ronsbo (1989)
Pekov et al. (2006)
Melluso et al. (2012)
Arden&Halden (1999)
Na
REE
Ca
b)
LREE3Ca2[SiO4]3Cl
Britholite
Na3LREE(PO4)2
Vitusite
Na
REE

Figure 6

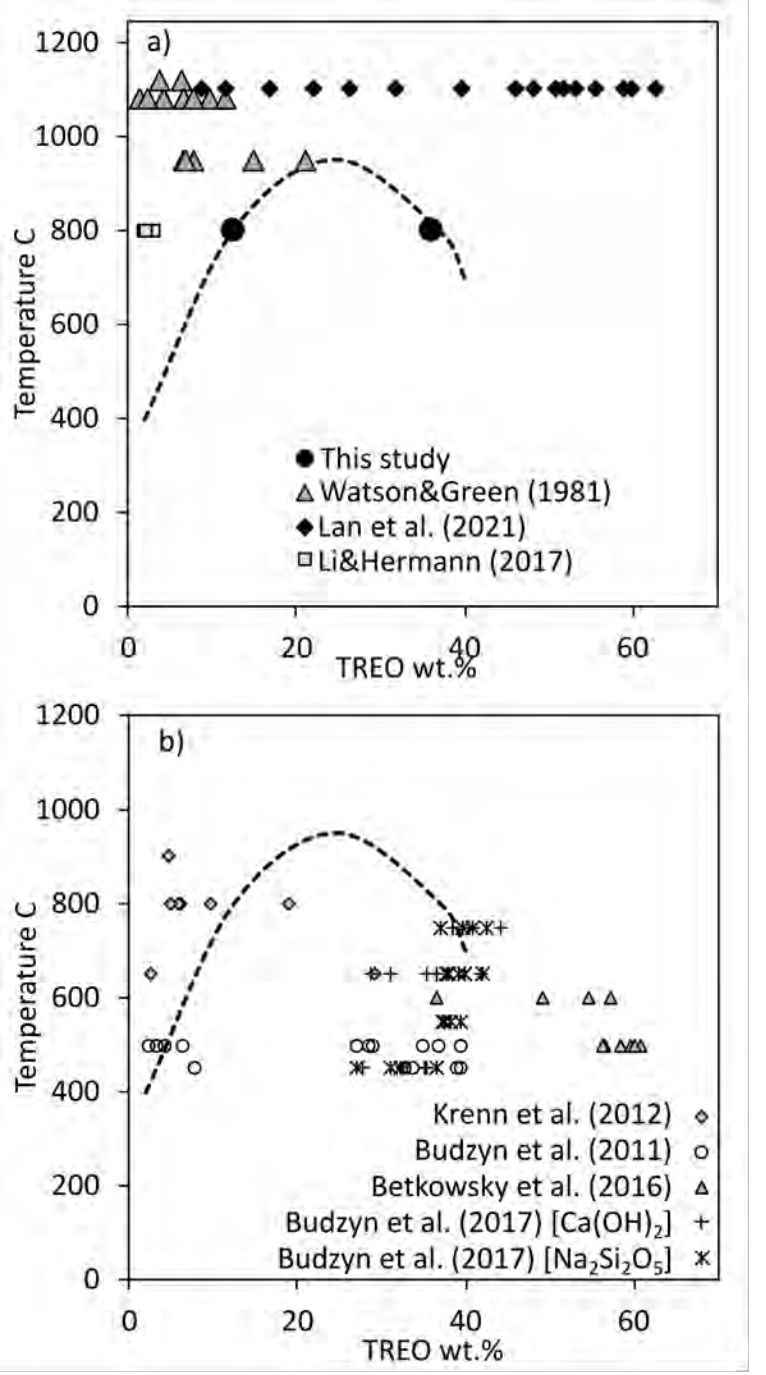
a)
Temperature C
TREO wt.%
This study
Watson&Green (1981)
Lan et al. (2021)
Li&Hermann (2017)
b)
Temperature C
TREO wt.%
Krenn et al. (2012)
Budzyn et al. (2011)
Betkowsky et al. (2016)
Budzyn et al. (2017) [Ca(OH)2]
Budzyn et al. (2017) [Na2Si2O5]

Figure 7

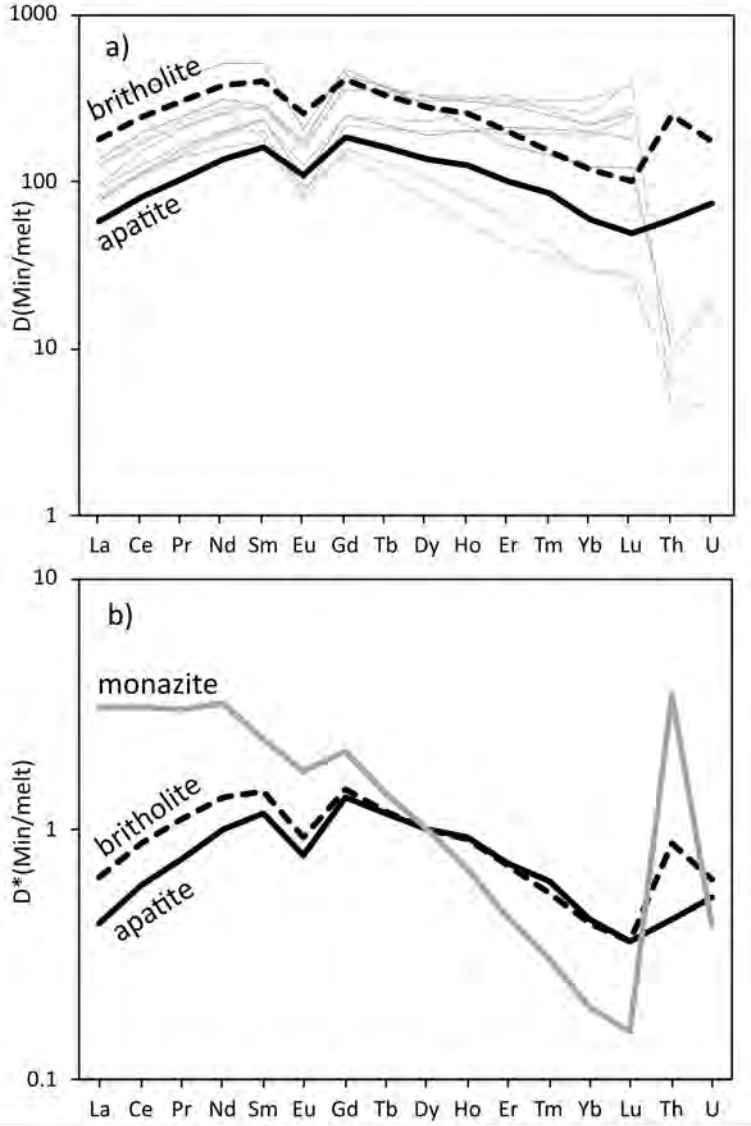
a)
britholite
apatite
D(Min/melt)
1000
100
10
1
La Ce Pr Nd Sm Eu Gd Tb Dy Ho Er Tm Yb Lu Th U
b)
monazite
britholite
apatite
D*(Min/melt)
10
1
0.1
La Ce Pr Nd Sm Eu Gd Tb Dy Ho Er Tm Yb Lu Th U

Figure 8